Advances in Geo-Energy Research

Vol. 14, No. 1, p. 64-80, 2024

Original article

Influencing mechanisms of multi-scale pore-fracture responses of coals on their macro/micromechanical behaviors under $ScCO_2$ injection

Qinghe Niu[1,2], Xinyi Wang[1,2], Jiangfang Chang[3]*, Wei Wang[1,2], Xudong Liu[4], Qizhi Wang[5]

[1]*Key Laboratory of Roads and Railway Engineering Safety Control (Shijiazhuang Tiedao University), Ministry of Education, Shijiazhuang 050043, P. R. China*

[2]*Hebei Technology and Innovation Center on Safe and Efficient Mining of Metal Mines, Shijiazhuang 050043, P. R. China*

[3]*Department of Engineering Mechanics, Shijiazhuang Tiedao University, Shijiazhuang 050043, P. R. China*

[4]*Bohai Bay Energy Research Institute, Northeast Petroleum University, Qinhuangdao 066000, P. R. China*

[5]*School of Civil Engineering, Hebei University of Science and Technology, Shijiazhuang 050018, P. R. China*

Keywords:
$ScCO_2$-water-coal reaction
nanoindentation
3D reconstruction
mechanical properties

Cited as:
Niu, Q., Wang, X., Chang, J., Wang, W., Liu, X., Wang, Q. Influencing mechanisms of multi-scale pore-fracture responses of coals on their macro/micromechanical behaviors under $ScCO_2$ injection. Advances in Geo-Energy Research, 2024, 14(1): 64-80. https://doi.org/10.46690/ager.2024.10.08

Abstract:
To decipher the mechanical response mechanisms of coal seams with multi-scale pore-fracture structure to supercritical CO_2 ($ScCO_2$) injection, two coal samples from different mines of the Ordos Basin, North China, were first selected for conducting $ScCO_2$-water-coal reaction experiments. Subsequently, the pore-fracture structure, macroscopic and microscopic mechanical behaviors of samples with different reaction times were analyzed, and the evolution patterns of pore-fracture parameters and relationships between the macroscopic and microscopic mechanical parameters were finally elucidated. The results showed that the $ScCO_2$-water-coal reaction modifies the pore-fracture structure in coal. Originally filled fractures re-open, original micro-fractures expand, new fractures form, and pores evolve from small- to large-sized. After the $ScCO_2$-water-coal reaction, the evolution of the compaction stage, the macroscopic mechanical parameters and the energy dissipation during loading corroborate the weakening effect of the $ScCO_2$-water-coal reaction on coal. The changes observed in the microscopic mechanical parameters align with those in the macroscopic mechanical parameters; however, due to the strong heterogeneity of coal and the inability of microscopic parameters to reflect the component and pore-fracture distribution, certain characteristics of the change amplitude of macroscopic and microscopic mechanical parameters of coal are inconsistent. The $ScCO_2$ extraction effect, the chemical dissolution, the different-sized pore-fracture evolution, the coupling effect of geostress, reservoir pressure, and swelling stress are the main factors to consider during the process of $ScCO_2$ sequestration in deep coal seams at the micro-, meso- and macro-scales, as they are responsible for potential safety issues.

1. Introduction

The injection of CO_2 into coal seams can efficiently replace or displace the coalbed methane (CBM), making it a promising strategy for enhancing CBM recovery (Busch and Gensterblum, 2011; Ji et al., 2017; Niu et al., 2022). Deep coal seam that is buried at depths greater than 1,000 m has considerable CO_2 storage potential and is an ideal location for carbon capture, utilization and storage. Under the conditions

Yandy Scientific Press

*Corresponding author.
E-mail address: qinghniu@163.com (Q. Niu); w_xinyi1999@163.com (X. Wang); changjiangfang@stdu.edu.cn (J. Chang); wangweiuuu@163.com (W. Wang); xudongliu_cumt@163.com (X. Liu); wangqizhi118@126.com (Q. Wang).
2207-9963 © The Author(s) 2024.
Received August 10, 2024; revised September 5, 2024; accepted September 27, 2024; available online October 2, 2024.

where deep coal seam occurs (reservoir pressure > 7.4 MPa, reservoir temperature > 31.1 °C), CO_2 is in the supercritical state (Wang et al., 2020a; Fu et al., 2023; Pan et al., 2024). The strong adsorption capacity of supercritical CO_2 ($ScCO_2$) can easily alter the mechanical properties of coal seams and their original stress state, resulting in additional displacement and deformation, which in turn leads to coal damage and triggers a series of potentially secondary hazards (CO_2 leakage, fault activation, site instability, etc.), altering the effectiveness of CO_2 geological sequestration (Anderson, 2017; Gholami et al., 2021; Song et al., 2023a). Thus, it is crucial to investigate the weakening characteristics of coal seams after $ScCO_2$ injection and the change mechanisms of their mechanical properties both at the macro- and microscopic level.

The two-phase mixture of gas and carbonic acid solution after injecting $ScCO_2$ into water can induce complex physical and chemical reactions in coal seams, leading to adsorption swelling, extraction and chemical dissolution/precipitation effects, ultimately changing the microstructure of coal. The phenomenon of adsorption swelling has been widely recognized in engineering sites and indoor experiments (Fujioka et al., 2010; Gor et al., 2017), and its causes have been linked to the extraction effect of $ScCO_2$ on the macromolecules of the coal matrix (Niu et al., 2021a). Coal contains multiple minerals and $ScCO_2$ dissolving in water generates hydrogen ions that can in turn dissolve carbonate minerals (Wang et al., 2020a; Zhou et al., 2021; Bekeshov et al., 2023). The formed carbonate ions can also combine with some cations to form precipitates (Anggara et al., 2013; Chang et al., 2017). The above CO_2-water-coal reactions can change the size, shape and distribution characteristics of the pore-fracture structure (Niu et al., 2021b; Song et al., 2023b; Li et al., 2024). In response to the CO_2-water-coal reaction, the pore volume of coal significantly increases (Liu and Rutqvist, 2010), particularly in micropores and mesopores ranging from 1.5 to 8 nm (Du et al., 2020). Moreover, the fractal dimension reduces, which indicates that the pore surface has become smooth and homogeneous (Zhang et al., 2021a). Similarly, the CO_2-water-coal reaction can not only promote fracture development through dissolution but also facilitate the formation of new fractures in the coal matrix (Sampath et al., 2019a, 2019b). However, the CO_2-water-coal reaction is extremely complex and its impact on pore-fracture structure is diverse. For example, the volume and quantity of some pores may also decrease after this reaction (Espinoza and Santamarina, 2017). The effect of CO_2-water-coal on pores in coal is also influenced by coal rank, as well as mineral composition and content (Ibrahim, 2022). As a limitation of previous studies, they have typically examined the pores and fractures of coal separately after the CO_2-water-coal reaction, without clarifying their interrelated effects.

Changes in the pore and fracture structure of coal due to $ScCO_2$ injection will inevitably affect its mechanical properties. Furthermore, changes in the mechanical properties of coal seams under geostress will influence the evolution of these pores and fractures (Sampath et al., 2018; Xue et al., 2020). It is generally believed that the $ScCO_2$-water-coal reaction can weaken the mechanical strength of coal-rock, reducing the compressive strength and elastic modulus by several to several tens of percent (Zhang et al., 2021b; Sang et al., 2022; Liu et al., 2023a). These mechanical parameters can show significant changes in the short term, although the change rate slows down as time progresses. The $ScCO_2$-water-coal reaction also enhances the deformation behavior of coal during the loading process, resulting in earlier crack propagation and failure (Zagorščak and Thomas, 2018; Jia et al., 2019). Simultaneously, these reactions alter the microscopic mechanical parameters of coal-rock, with significant reductions observed in the microscopic Young's moduli and hardness after the $ScCO_2$-water-coal reaction (Wang et al., 2024). However, these parameters are dependent on the composition and microstructure of coal (Liu et al., 2022). Numerous studies have confirmed the softening effect of $ScCO_2$ injection on coal seams and provided substantial evidence of this phenomenon (Zhang et al., 2022a, 2022b; Otu et al., 2023). Much of the focus has been on the impact of the $ScCO_2$-water-coal reaction on the elastic modulus and compressive strength of coal-rock, while research has been insufficient on other mechanical parameters such as cohesion and internal friction angle. At the same time, studies on how the pore-fracture structure of coal influences the relationship between macroscopic and microscopic mechanical parameters remain scarce, limiting our understanding of the mechanisms behind the mechanical weakening of coal seams under $ScCO_2$ injection. Additionally, researches have predominantly centered on the highly metamorphic anthracite, while relatively less emphasis has been placed on medium- and low-rank coals, particularly those rich in minerals, restricting our knowledge on the safety of $ScCO_2$ sequestration in different coal seams.

This work intends to reveal the multi-scale structural response and macro/micromechanical behavior evolution of coals after $ScCO_2$ injection, as well as clarify the inherent change mechanism of microstructure on the macro/micromechanical strength and deformation characteristics, aiming to provide a scientific basis for appropriate site selection and safety evaluation of $ScCO_2$ sequestration in coal seams.

2. Experiments

2.1 Sample collection and preparation

To assess the safety of CO_2 sequestration in coal seams from various mining areas in the Ordos Basin, the Wulan coal mine (Inner Mongolia) and the Yuheng mining area (Shaanxi Province), situated at the eastern and northeastern edges of the Ordos Basin, were chosen as the research areas. The representative coal samples were collected underground (Fig. 1). According to the classification method in the Chinese National Standard (GB5751-86), coal samples from the Wulan coal mine (NM sample) and the Yuheng coal mine (SX sample) belong to coking coal and gas coal (Wang et al., 2020b), respectively.

Prior to the experimental tests, the collected coal samples were prepared into standard cylindrical samples measuring 25 mm × 50 mm, flat cylindrical samples with a diameter of 25 mm and a height of 5 to 8 mm, and powder samples with a particle size of less than 300 mesh. To reduce the discreteness of the nanoindentation test results, the flat cylindrical samples

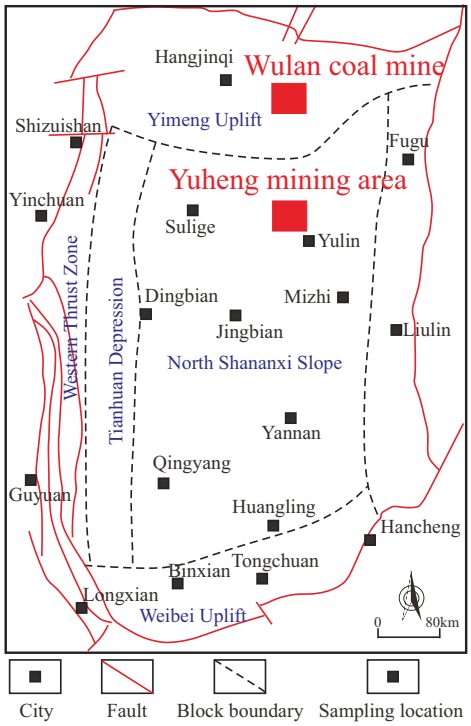

Fig. 1. Sample location (Chen et al., 2024).

were processed with 300-mesh, 800-mesh, and 1,500-mesh sandpaper in sequence and polished with oil-based diamond suspension to ensure that the unevenness was controlled within 0.05 mm. To avoid the discreteness of the mechanical property testing results, the acoustic velocity of samples was measured, and samples with a difference of less than 5% in acoustic velocity were selected as the test objects.

2.2 Basic information of samples

In accordance with the Chinese National Standards GB/T1528-2017 and GB/T212-2008, coal samples underwent whole rock composition analysis and proximate analysis using X-ray Diffraction and an industrial analyzer (Tables 1 and 2). Significant differences can be found in the microscopic composition of NM and SX samples. The SX sample has higher organic carbon content (97.0%), while the remaining components are mainly quartz and kaolinite. On the contrary, the organic carbon content of the NM sample is relatively low (64.4%), and abundant carbonate minerals (35.3%) are developed. Thus, the moisture and volatile matter in the SX sample are higher than those in the NM sample, while the ash yield and fixed carbon content are both lower than those in sample NM.

2.3 Experimental and testing methods

To analyze the response characteristics of the pore-fracture structure and the mechanical properties of coal seams in response to $ScCO_2$ injection, the $ScCO_2$ geological sequestration process under in-situ temperature and pressure conditions was first simulated using a gas-liquid-solid high-temperature and high-pressure reactor. Then, the internal pore-fracture structure of samples was scanned and reconstructed via micro-CT. Finally, the macroscopic and microscopic mechanical properties of samples were tested using a rock triaxial multi-field coupling test system and a nanoindentation experiment.

Table 1. Proportions of organic carbon and major minerals in the studied coal samples.

No.	Organic carbon (%)	Quartz (%)	Kaolinite (%)	Calcite (%)	Dolomite (%)
NM	64.4	0.3	-	30.5	4.8
SX	97.0	0.8	2.2	-	-

Notes: -, under detection limit.

Table 2. Proximate analysis of the studied coal samples.

No.	Moisture (%)	Ash yield (%)	Volatile (%)	Fixed carbon (%)
NM	0.92	19.62	13.84	68.47
SX	4.40	3.66	30.47	63.93

2.3.1 $ScCO_2$-water-coal reaction experiment

The gas-liquid-solid high-temperature and high-pressure reactor has a maximum operating temperature of 150 °C and a maximum operating pressure of 60 MPa. To simulate the in-situ temperature and pressure conditions of coal seams, the relationship between reservoir pressure (P_p), reservoir temperature (T), and reservoir buried depth (D) was referenced as follows (Meng et al., 2011; Jia, 2017):

$$\begin{aligned} P_p &= 0.0122D - 2.8886 \\ T &= 0.032D + 9.4444 \end{aligned} \quad (1)$$

To reflect the characteristics of deep coal seams, reservoir conditions at a burial depth of 1,000 m ($P_p = 9.31$ MPa, $T = 41.4$ °C) were selected as experimental parameters. Previous studies suggest that the weakening of the mechanical strength of coal by $ScCO_2$ erosion during the long-term process is mainly concentrated to the initial stage (Perera et al., 2013; He et al., 2024). Thus, the reaction time of the $ScCO_2$-water-coal reaction was set at 7 and 14 d in this work

2.3.2 CT scanning and 3D reconstruction

The μ-CT (Phoenix Vtomex L300 nano/micro-CT, General Electric, Inc., United States) was used to scan samples before and after the $ScCO_2$-water-coal reaction. The main parameters of micro-CT scanning were a spatial resolution of 27 μm, scanning voltage of 120 KV, and scanning current of 120 μA. First, the scanned slice images were filtered using the median filtering method to reduce noise and improve image clarity. Next, a large number of two-dimensional slices were cropped, grayscale was adjusted, volume data were edited, threshold was segmented, and three-dimensional reconstruction was performed to obtain a microstructure spatial distribution feature map. The threshold parameter deviation for different segmentation thresholds was set to less than 1%, ensuring the reliability of the result. Finally, the key parameters within

samples were extracted, calculated, screened, and statistically analyzed to examine the impact of the $ScCO_2$-water-coal reaction on the pore-fracture structure of the samples.

2.3.3 Testing of macroscopic mechanical properties

The macroscopic mechanical properties of samples were measured using a rock triaxial multi-field coupling test system, which has a maximum injection pressure of 60 MPa, a maximum axial load of 1,000 kN, and a maximum control temperature of 150 °C. The measurement accuracy for pressure and temperature was 0.01 MPa and 0.01 °C, respectively. The measurement accuracy for axial and radial deformation was less than 1% FS. The testing process comprised the following steps:

1) Place samples before or after the $ScCO_2$-water-coal reaction into the sample room and install LVDT and circumferential extensometers;
2) Conduct loading-deformation-failure tests on coal samples under no confining pressure, 5 and 10 MPa confining pressures. Apply the axial stress by the displacement control method, and set the loading speed to 0.1 mm/min;
3) Monitor the axial and radial strains during the experimental process in real time, observe the morphology of samples after failure, and analyze the influence of $ScCO_2$-water-coal reaction on the macro-mechanical behavior of coal.

2.3.4 Testing of microscopic mechanical properties

Microscopic mechanical property testing was conducted using the Anton Paar nanoindenter model TTX-NHT2 (Anton Paar GmbH, Graz, Austria). The maximum effective load was ≥ 500 mN with a resolution of ≤ 40 nN, the maximum indentation depth was ≥ 200 μm, and the displacement resolution was ≤ 0.004 nm. During the experiment, three points were taken from each sample, and the force-controlled loading mode was adopted. The loading was first applied at a speed of 40 mN/min, then held for 20 s when the maximum load was reached, and finally, the same speed was used to unload the stress. Based on the measured load-depth curve, the microscopic mechanical characteristics of samples were analyzed at the nanomechanical scale.

The Oliver-Harr rule was implemented in analyzing the load-depth curve (Ma et al., 2020). With the continuous application of load, the indentation depth gradually increases and the sample exhibits coexisting deformation characteristics of elasticity and plasticity. Afterwards, the indentation depth is independent of the load but increases with time when entering the maintain load stage. Finally, the indentation depth recovers to a certain extent as the load decreases during the unloading phase, and there is a residual indentation depth due to the plastic characteristic.

The load-depth curve in the unloading stage is commonly described by a simple power function:

$$F_n = \alpha(h - h_p)^{\beta} \tag{2}$$

where F_n represents the load, h represents the contact displacement, h_p is the residual indentation depth, and the constants α and β are fit parameters. The contact stiffness (S) can be determined from the slope of the unloading curve:

$$S = \left(\frac{\mathrm{d}F_n}{\mathrm{d}h}\right)_{h=h_{\max}} = \alpha\beta(h_{\max} - h_p)^{\beta-1} \tag{3}$$

The indentation hardness (H_{IT}) and equivalent modulus (E_r) can be obtained by the following equation:

$$H_{IT} = \frac{F_m}{A} \tag{4}$$

$$E_r = \frac{S\sqrt{\pi}}{2\eta\sqrt{A}} \tag{5}$$

where F_m is the maximum load, A represents the contact area between the indenter and the sample; η represents a constant related to the shape of the indenter, the Berkovich indenter is used, and $\eta = 1.034$. The indentation elastic modulus E_{IT} is expressed as:

$$E_{IT} = \frac{1 - \upsilon_{IT}^2}{\frac{1}{E_r} - \frac{1 - \upsilon_c^2}{E_c}} \tag{6}$$

where υ_{IT} represents the Poisson's ratio of samples, and E_c and υ_c represent the elastic modulus and Poisson's ratio of indenters, respectively; $E_c = 1,141$ GPa, $\upsilon_c = 0.07$.

3. Results and discussion

3.1 Influence of $ScCO_2$-water-coal reaction on the pore-fracture structure of coal

3.1.1 Layered surface porosity

Based on nearly 1,500 two-dimensional grayscale image slices from the CT scans, the layered surface porosity was calculated by the ratio of pore area to the entire slice area. The layered surface porosity of samples with different $ScCO_2$-water-coal reaction times is shown in Fig. 2. The strong heterogeneous characteristics of coal samples result in significant variation in the surface porosity across different sections.

For the NM sample without $ScCO_2$-water-coal reaction, the layered surface porosity is 0.007-0.104, which then increases to 0.014-0.243 and 0.023-0.314 after $ScCO_2$-water-coal reaction of 7 and 14 d.

For the SX sample without the $ScCO_2$-water-coal reaction, the layered surface porosity ranges from 0.016 to 0.048. This increases to 0.061 to 0.251 and 0.099 to 0.313 after the $ScCO_2$-water-coal reaction for 7 and 14 d, respectively. The $ScCO_2$-water-coal reaction has a pore-enlargement effect for coals, albeit it has different contribution degrees in various regions of the sample. Obviously, the pore-enlargement effect is strongly reflected in the bottom and middle of the NM sample, while it is equally present in the bottom, middle and top of the SX sample. These results confirm the microheterogeneity inside different coals. To describe the degree of heterogeneity of porosity along the coal core axis direction, the coefficient of variation (CV) was adopted. The results show that when the $ScCO_2$-water-coal reaction time increases from 0, 7 to 14 d, the CV of the layered surface porosity of the NM sample is 0.64, 0.63 and 0.52, respectively, while the CV of the layered

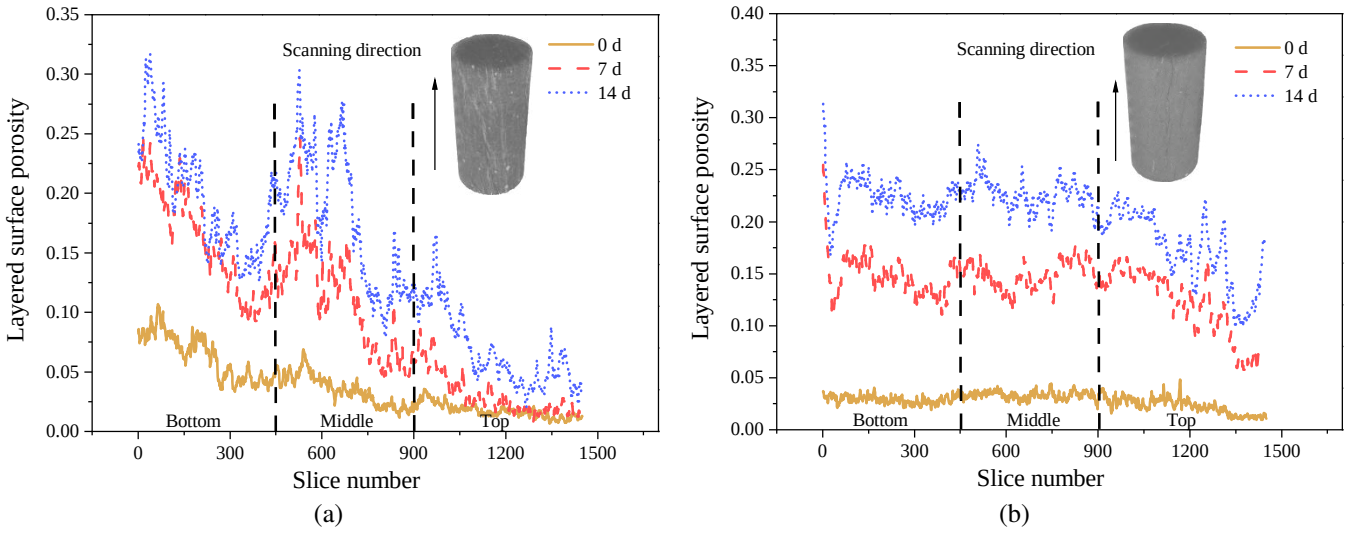

Fig. 2. Layered surface porosity of samples with different $ScCO_2$-water-coal reaction times. (a) and (b) represent NM and SX samples, respectively.

surface porosity of the SX sample is 0.25, 0.19 and 0.17, respectively. This has two meanings: (1) The heterogeneity of the NM sample is stronger than that of the SX sample; (2) the $ScCO_2$-water-coal reaction reduces the difference in pore distribution in samples, resulting in a greater uniformity of pores.

3.1.2 Fracture characteristic response

The fracture morphology of samples under different $ScCO_2$-water-coal reaction times is shown in Fig. 3. The distribution of internal fractures in samples after the $ScCO_2$-water-coal reaction is influenced by the original fracture characteristics and controlled by physical and chemical reactions. The NM sample contains more soluble minerals (such as calcite), and the $ScCO_2$ aqueous solution causes the dissolution of soluble minerals and induces the generation of new fractures, such as corrosion fractures intersecting obliquely with the sample axis. In contrast, as the SX sample has fewer soluble minerals, it is difficult for large-scale dissolution fractures to develop. The formation of associated fractures around large fractures may be related to the dissolution effect. Additionally, bedding exists between different components of coal (such as bright coal bands and dark coal bands), which forms weak planes in coal seams when the bonding is weak. The coal matrix can adsorb a large amount of $ScCO_2$, causing matrix swelling deformation with a volume swelling strain of up to 3%. This periodic swelling and contraction deformation of the matrix leads to spalling phenomena in samples, forming fractures (swelling-induced fractures) with strong connectivity in the bedding direction. Compared to the NM sample, the SX sample contains more organic matter with stronger $ScCO_2$ adsorption capability, resulting in the formation of several parallel swelling-induced fractures. It should be noted that after 7 days of $ScCO_2$-water-coal reaction, the structure of dissolution fractures and swelling-induced fractures within the samples is initially formed. With the reaction time extended, the main fractures remain unchanged, while more associated small fractures are generated in the surroundings.

The fracture parameters of samples under varying $ScCO_2$-water-coal reaction times are shown in Fig. 4. As the $ScCO_2$-water-coal reaction time extends from 0, 7 to 14 d, the average fracture length of NM sample and SX sample increases by 217.06%-223.18% and 192.98%-219.67%, respectively, the average fracture aperture increases by 203.85%-213.57% and 123.91%-142.59%, respectively, and the quantity density increases by 369.74%-494.63% and 339.12%-504.08% respectively. These data confirm the promoting effect of $ScCO_2$-water-coal reaction on fracture expansion and generation.

Regarding the distribution characteristics of fracture size parameters, the $ScCO_2$-water-coal reaction increases the number of fracture types, allowing micro-fractures, branch fractures, and main fractures to coexist, thus enhancing the complexity of the fracture network. Moreover, after the $ScCO_2$-water-coal reaction, the evolution of internal fractures in the NM sample is simultaneously controlled by chemical dissolution and swelling deformation. As a result, the increase in fracture length and aperture of the NM sample is greater than that of the SX sample, providing a dual promoting effect on fracture extension in samples.

3.1.3 Pore characteristic response

The pore distribution of samples under different $ScCO_2$-water-coal reaction times is shown in Fig. 5. It can be seen that the internal pores of both NM and SX samples show strong non-uniform distribution characteristics before and after the $ScCO_2$-water-coal reaction. This can be primarily attributed to the complexity of organic and mineral components within samples. Interestingly, there is also a certain relationship between the non-uniform distribution of pores and the spatial distribution of fractures. On the one hand, the presence of fractures increases the permeability in their extension direction, promoting the interaction between $ScCO_2$, water and

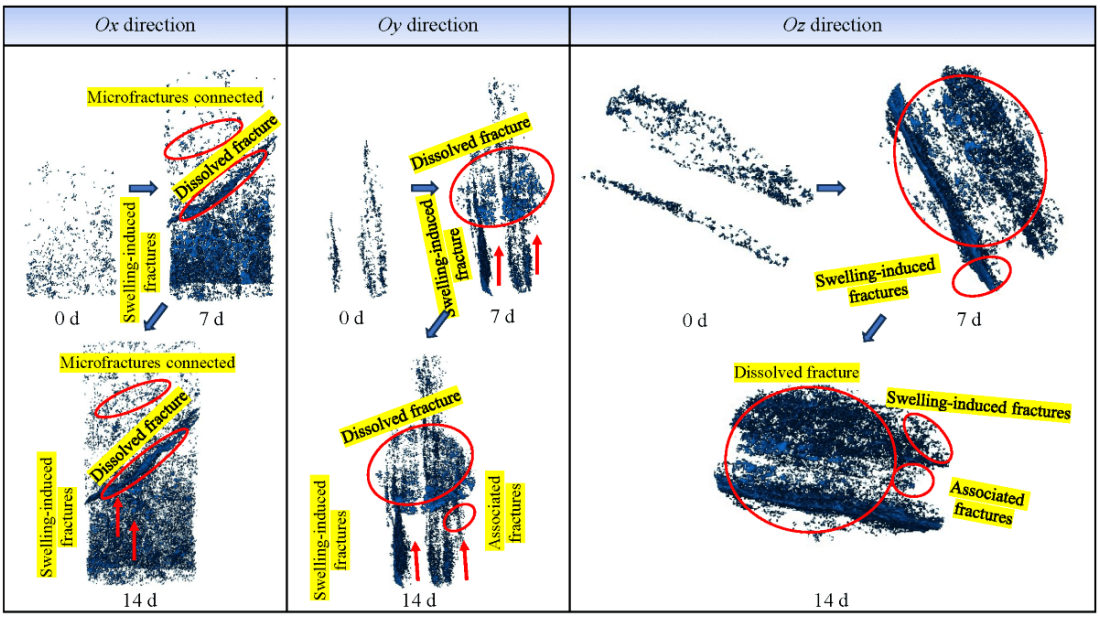

(a)

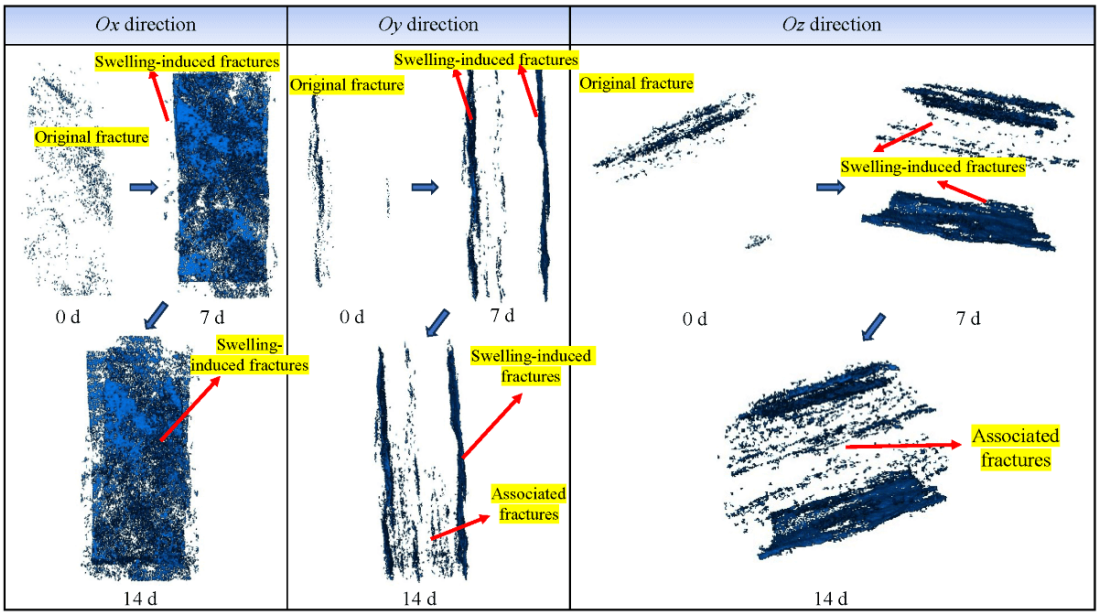

(b)

Fig. 3. Fracture morphology of samples under different $ScCO_2$-water-coal reaction times. (a) and (b) represent NM and SX samples, respectively.

coal, resulting in chemical dissolution and adsorption-induced swelling/contraction deformation around the fractures, which in turn lead to the generation of more pores (such as pore clusters along the fracture axis direction in NM and SX samples). On the other hand, the formation of fractures leads to preferential flow, restricting the $ScCO_2$-water-coal reaction perpendicular to the fracture surface direction, causing pores to accumulate in localized areas within samples (such as the pore clusters observed below oblique intersecting fractures in the NM sample).

In order to thoroughly analyze the impact of $ScCO_2$-water-coal reaction on different types of pores, according to pore volume, pores were divided into: Ultra-macropores (pore volume $> 1 \times 10^8$ μm^3), macropores (1×10^7 μm^3 $<$ pore volume $< 1 \times 10^8$ μm^3), mesopores (1×10^6 μm^3 $<$ pore volume $< 1 \times 10^7$ μm^3), transitional pores (1×10^5 μm^3 $<$ pore volume $< 1 \times 10^6$ μm^3), and micropores (pore volume $< 1 \times 10^5$ μm^3). The pore number density, porosity and their percentages in samples under different $ScCO_2$-water-coal reaction times are shown in Fig. 6.

It can be found that the number of micropores and transition pores in samples before and after the $ScCO_2$-water-

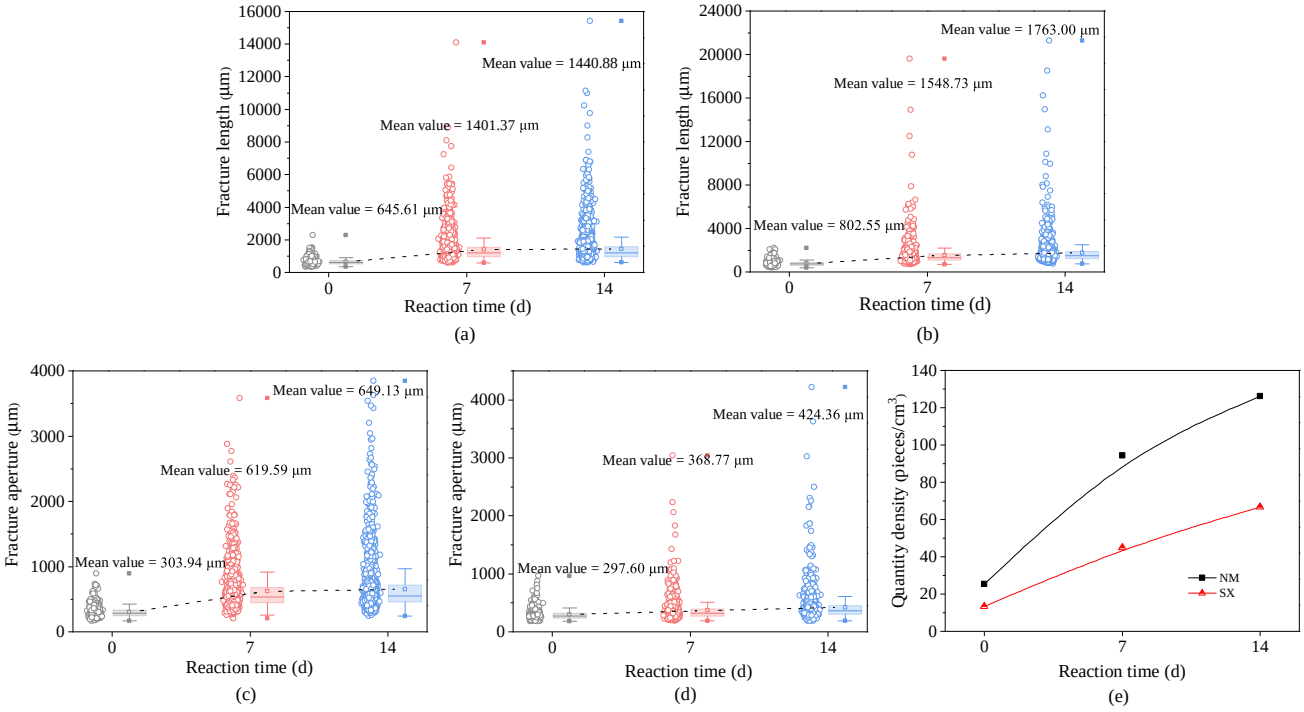

Fig. 4. The fracture parameters of samples under different $ScCO_2$-water-coal reaction times. (a) and (b) represent the fracture length of NM and SX samples, respectively; (c) and (d) represent the fracture aperture of NM and SX samples, respectively; (e) represent the quantity density of NM and SX samples.

coal process is the highest, followed by mesopores, while the number of macropores and ultra-macropores is the lowest. The $ScCO_2$-water-coal reaction does not fundamentally change the overall distribution of pores in samples. All pores of samples after the $ScCO_2$-water-coal reaction increase in number, while the proportion of different pore number densities varies. The number of micropores and transition pores is observed to decrease after the $ScCO_2$-water-coal reaction, while the number of mesopores, macropores and ultra-macropore increases, reflecting that chemical dissolution and matrix swelling/contraction mainly induce the transformation of macropores or promoted the expansion of small pores to form large pores.

Contrary to the pore number density, the porosity of different-sized pores was arranged in descending order as follows: Ultra-macropores > macropores > mesopores > transition pores > micropores. Same as the pore number density, both the NM and SX samples show the same trend as the reaction time progresses, i.e., the porosity of all pores increases, with the ultra-macropore showing the most significant increase. Additionally, the porosity proportion of micropores, transition pores, mesopores, and macropores decreases, while the porosity of ultra-macropores increases. This further confirms that the $ScCO_2$-water-coal reaction has the most significant impact on ultra-macropores. In other words, the $ScCO_2$-water-coal reaction can significantly damage the internal structure of samples, thereby affecting their macro- and microscopic mechanical properties.

3.2 Influence of $ScCO_2$-water-coal reaction on macroscopic mechanical behavior of coal

3.2.1 Stress-strain curve

The stress-strain curves of samples under varying $ScCO_2$-water-coal reaction times are presented in Fig. 7. These curves display distinct stages: Compaction stage, elastic stage, yield stage, and post-peak stage (Wei et al., 2023; Xu et al., 2024). Among the different confining pressures and $ScCO_2$-water-coal reaction times, the most representative one is the compaction stage during the deformation-failure process of samples. The stress-strain curve of samples after the $ScCO_2$-water-coal reaction shows a concave trend, which becomes more pronounced with the reaction time extending. This is because the $ScCO_2$-water-coal reaction induces the generation of numerous fractures and pores, causing the samples to undergo irreversible deformation via the compression of pore-fracture structure during the loading process. Additionally, after applying confining pressure, the compaction stage is not significant as the pre-applied load has already compressed or closed the pores and fractures within the samples.

After the $ScCO_2$-water-coal reaction, the samples still exhibit a noticeable elastic stage, while the stress-strain curve becomes smoother, with this trend becoming more pronounced with a longer reaction time. This observation indicates that the $ScCO_2$-water-coal reaction can lead to the greater deformation of samples, altering their mechanical behavior. Furthermore, increasing the confining pressure has a certain strengthening effect on the mechanical properties of samples, which can suppress the mechanical weakening effect of the $ScCO_2$-water-

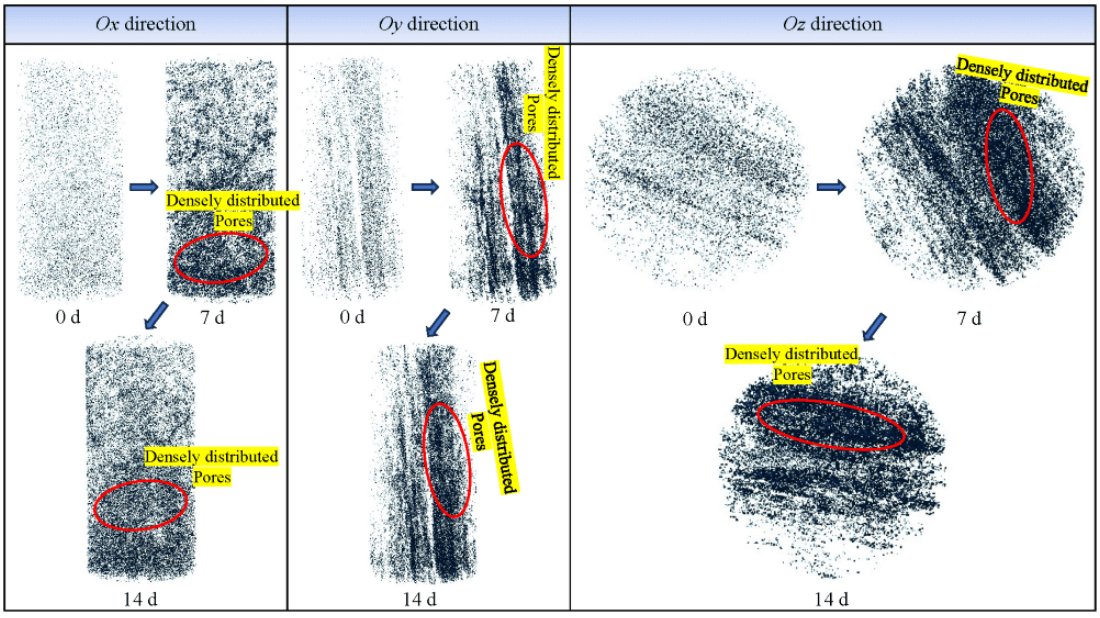

(a)

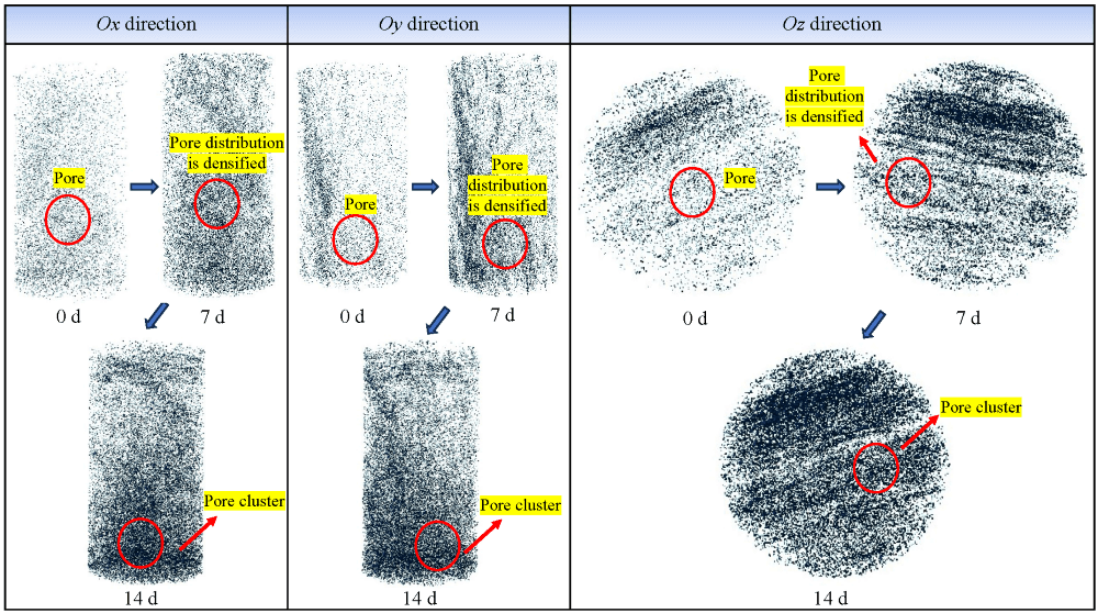

(b)

Fig. 5. Pore distribution in samples under different $ScCO_2$-water-coal reaction times. (a) and (b) represent NM and SX samples, respectively.

coal reaction. The samples after the $ScCO_2$-water-coal reaction exhibit a longer duration of yield stage and produce greater strain, along with the brittle-ductile transition in occurring in the samples, manifested by a decrease or disappearance of fracturing sounds as the $ScCO_2$-water-coal reaction time progresses.

After reaching the peak strength, the samples are suddenly destroyed, causing a drop in the stress-strain curve. Since the post-peak stage is uncontrollable in the experiment, the characteristics of the stress-strain curve after the $ScCO_2$-water-coal reaction are discussed no further.

3.2.2 Macroscopic mechanical parameters

The peak strength (G), elastic modulus (E), Poisson's ratio (μ), internal friction angle (ϕ), and cohesion (c) were selected as characteristic parameters for describing the macroscopic mechanical properties, whose evolution laws after the $ScCO_2$-water-coal reaction are shown in Fig. 8.

After the $ScCO_2$-water-coal reaction, the mechanical parameters of the NM and SX samples show systematic changes, reflected in the decrease in peak strength, elastic modulus, cohesion, and internal friction angle, while the Poisson's ratio increases. The peak strength of the NM and SX samples

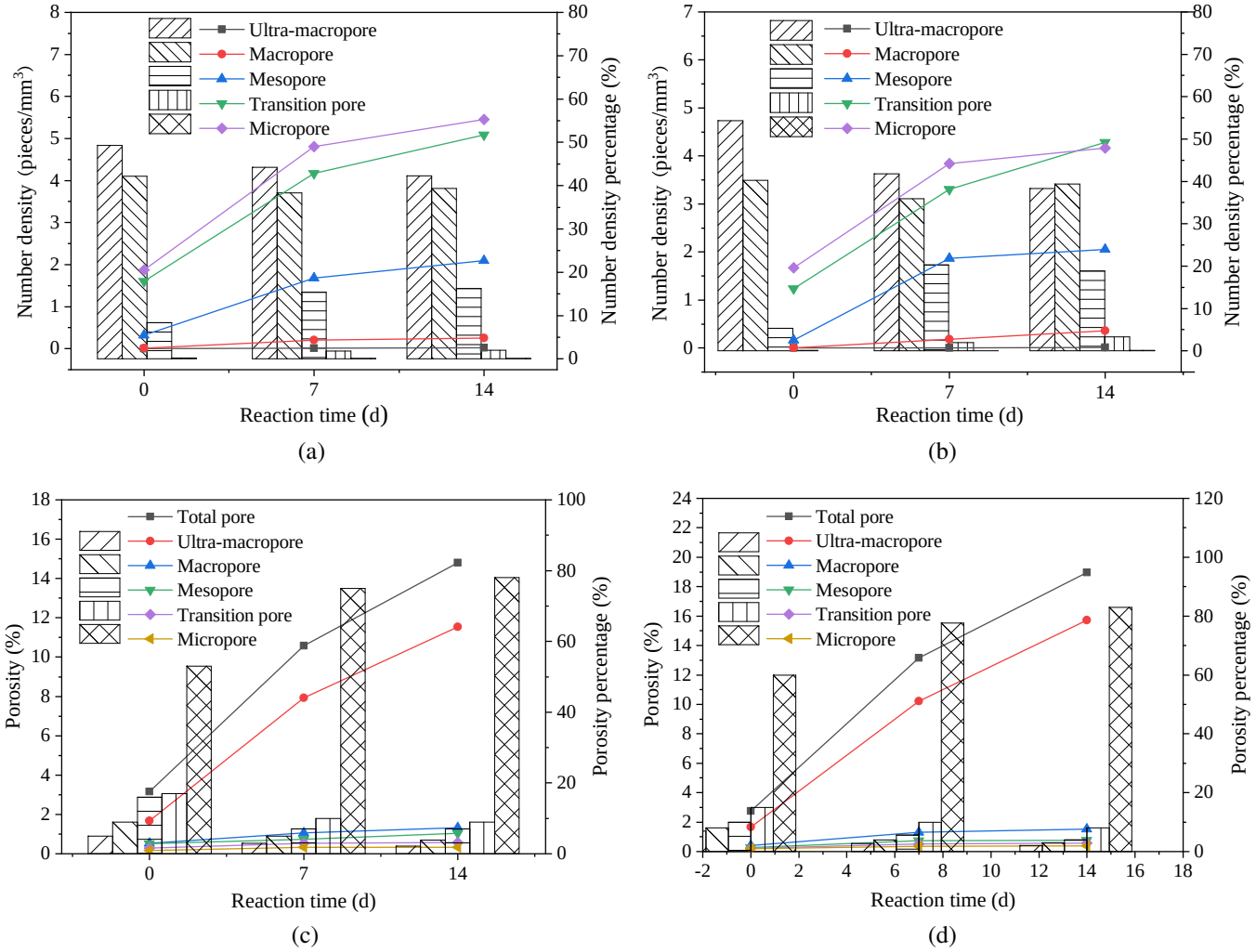

Fig. 6. Pore number density, porosity and their percentages in samples under different $ScCO_2$-water-coal reaction times. (a) and (c) represent the NM sample, (b) and (d) represent the SX sample.

without confining pressure decreases by 21.87%-31.06% and 20.32%-29.69%, respectively, the elastic modulus decreases by 37.95%-50.21% and 20.66%-35.41%, respectively, and the Poisson's ratio increases by 38.10%-52.38% and 3.03%-15.15%, respectively. The impact of the $ScCO_2$-water-coal reaction on the peak strength, elastic modulus and Poisson's ratio of the NM sample is more significant due to the presence of additional pores and fractures, which facilitate the development of internal fractures during loading. Under confining pressure, the peak strength and elastic modulus of samples are higher, indicating that the stress can enhance the mechanical performance of coal reservoirs during the $ScCO_2$ sequestration process. The decrease in the cohesion of the NM and SX samples after the $ScCO_2$-water-coal reaction is 16.49%-23.26% and 10.90%-19.63%, respectively, while the decrease in the internal friction angle is 4.15%-7.49% and 7.36%-9.14%, respectively. Compared to the SX sample, the NM sample has a greater decrease in cohesion and a smaller decrease in internal friction angle. This is because during the $ScCO_2$-water-coal reaction, the SX sample mainly undergoes chemical dissolution, leading to the failure of bonding between organic matter and minerals, whereas the NM sample mainly experiences swelling/contraction damage, causing mutual squeezing and interlocking of internal micro-particles. In conclusion, the differences in the composition and original structure of the NM and SX samples are the fundamental reasons for the inconsistency in their mechanical parameters.

3.2.3 Energy evolution characteristics

During the deformation and failure process under loading, the sample experiences energy input, accumulation and release, indicating its load-bearing capacity and brittle-ductile characteristics. Assuming that no heat exchange occurs with the external environment during this process, the energy composition of the samples can be determined according to the first law of thermodynamics:

$$U = U_e + U_d \tag{7}$$

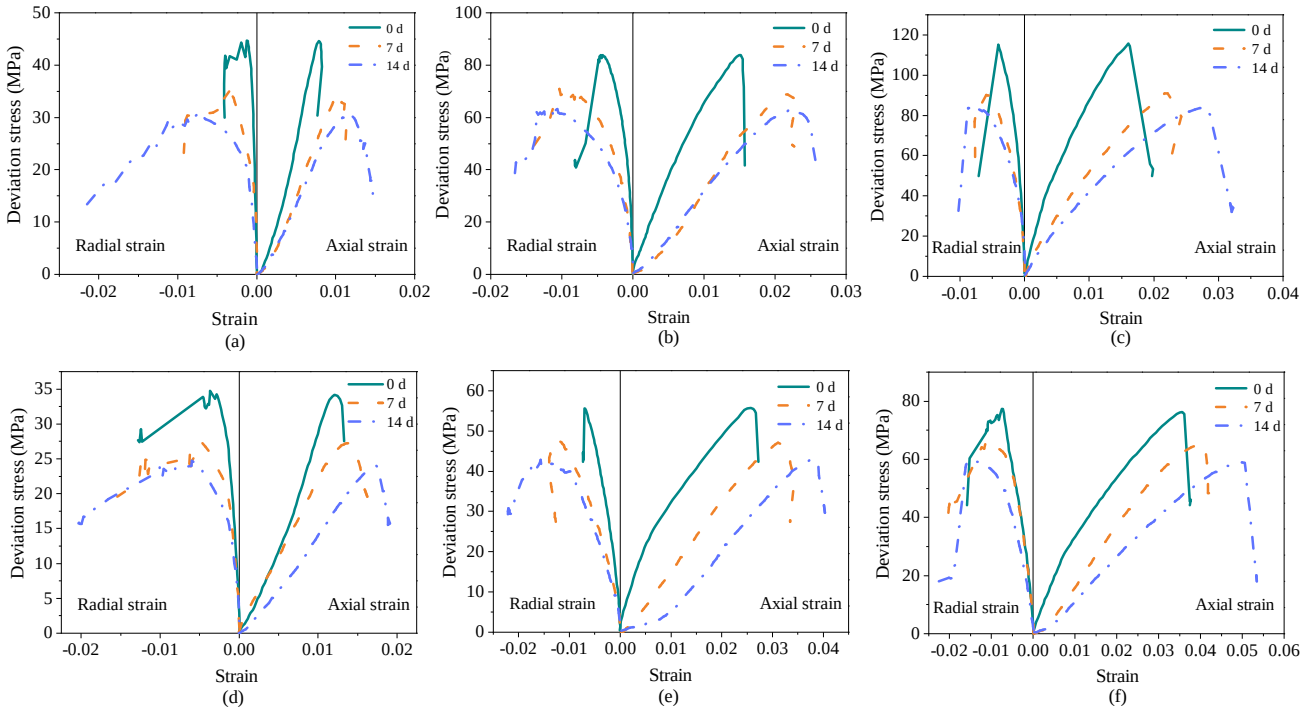

Fig. 7. Stress-strain curves of samples under different $ScCO_2$-water-coal reaction times. (a), (b) and (c) represent the NM sample under conditions of no confining pressure, 5 MPa confining pressure and 10 MPa confining pressure, respectively; (d), (e) and (f) represent the SX sample under conditions of no confining pressure, 5 MPa confining pressure and 10 MPa confining pressure, respectively.

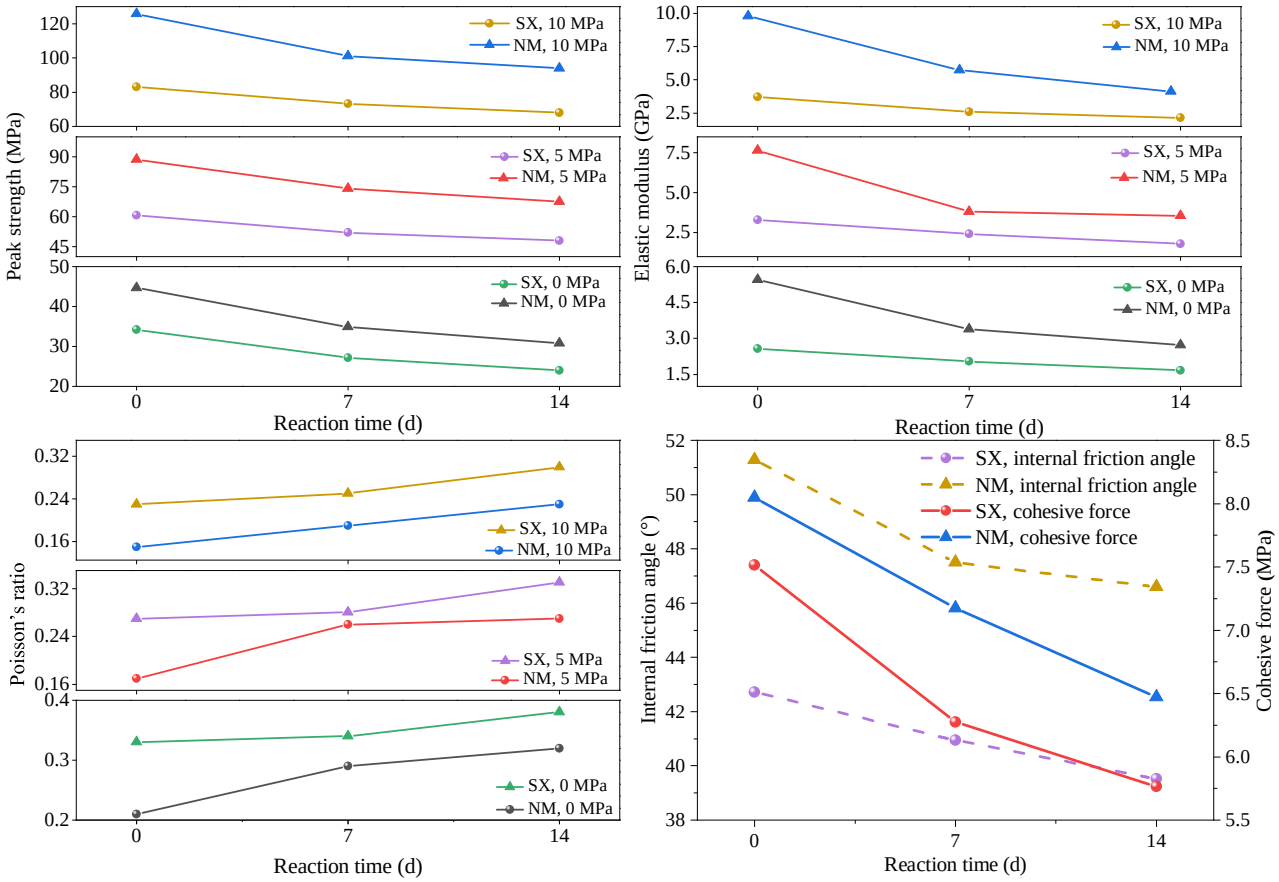

Fig. 8. Macroscopic mechanical parameters of samples under different $ScCO_2$-water-coal reaction times.

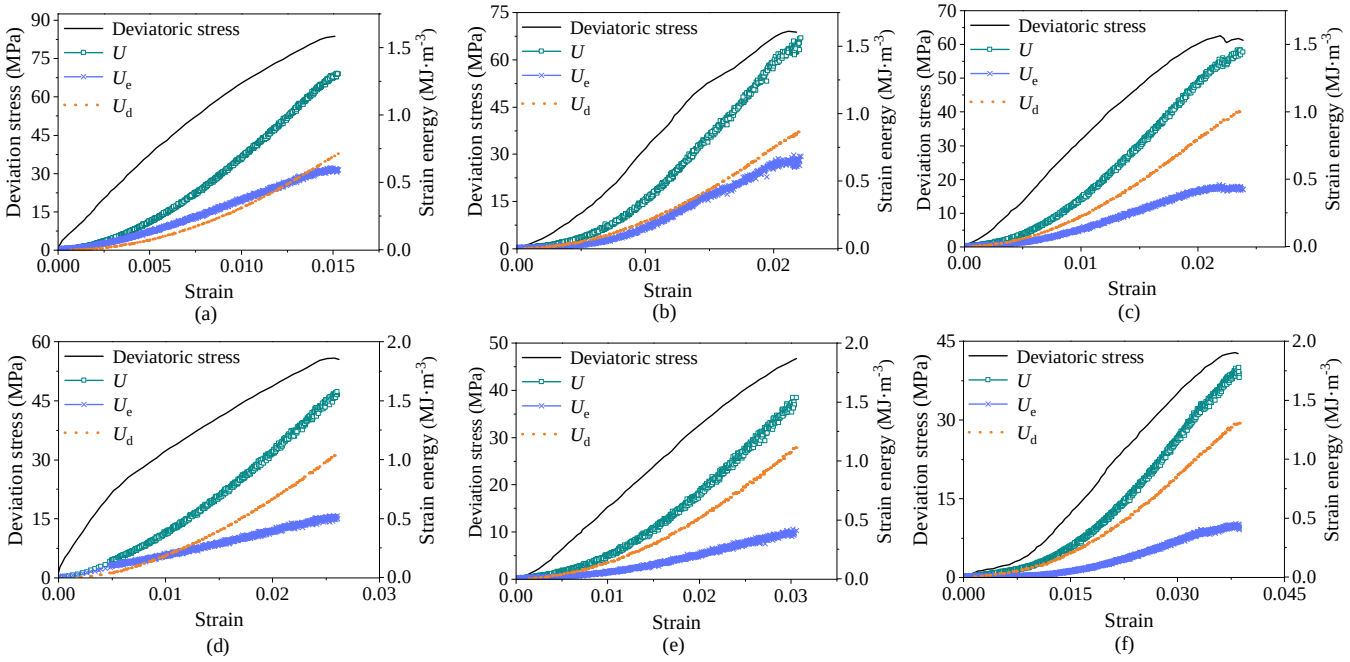

Fig. 9. Elastic energy and dissipative energy evolution of samples with $ScCO_2$-water-coal reaction. (a), (b) and (c) represent the NM sample with reaction times of 0, 7 and 14 d, respectively; (d), (e) and (f) represent the SX sample with reaction times of 0, 7 and 14 d, respectively.

where U represents the total energy generated by the work done by external forces; U_e and U_d respectively denote the elastic energy and dissipated energy of sample under the external force. Under complex stress conditions, U and U_e in the principal stress space can be expressed as:

$$U = \int_0^{\varepsilon_1} \sigma_1 \mathrm{d}\varepsilon_1 + \int_0^{\varepsilon_2} \sigma_2 \mathrm{d}\varepsilon_2 + \int_0^{\varepsilon_3} \sigma_3 \mathrm{d}\varepsilon_3 \tag{8}$$

$$U_e = \frac{1}{2E}\left[\sigma_1^2 + \sigma_2^2 + \sigma_3^2 - 2\mu(\sigma_1\sigma_2 + \sigma_1\sigma_3 + \sigma_2\sigma_3)\right] \tag{9}$$

where σ_1, σ_2 and σ_3 denote the maximum, intermediate and minimum principal stress of the sample, respectively; ε_1, ε_2, and ε_3 are the strains corresponding to the principal stress. In the conventional triaxial test process, if the confining pressure $\sigma_2 = \sigma_3$, Eqs. (8) and (9) can be rewritten as follows:

$$U = \int_0^{\varepsilon_1} \sigma_1 \mathrm{d}\varepsilon_1 + 2\int_0^{\varepsilon_3} \sigma_3 \mathrm{d}\varepsilon_3 \tag{10}$$

$$U_e = \frac{1}{2E}\left[\sigma_1^2 + \sigma_2^2 + \sigma_3^2 - 2\mu(2\sigma_1\sigma_3 + \sigma_3^2)\right] \tag{11}$$

Based on Eqs. (7), (10) and (11), the total energy, elastic energy and dissipated energy can be calculated.

The elastic and dissipative energy evolutions of samples undergoing the $ScCO_2$-water-coal reaction are illustrated in Fig. 9. As loading continues, both the elastic and dissipative energies of the samples gradually increase, with a sharp rise occurring once the strain surpasses 0.01. Meanwhile, the $ScCO_2$-water-coal reaction alters the evolution of these energies. Before the $ScCO_2$-water-coal reaction, the elastic energy of the sample initially exceeds the dissipative energy in the early stages of loading. However, as loading continues, the dissipative energy increases and eventually surpasses the elastic energy. During the $ScCO_2$-water-coal reaction, the dissipative energy remains higher than the elastic energy throughout the loading process, with the gap between the two widening as the reaction time expands. The increase in dissipative energy after the $ScCO_2$-water-coal reaction can be attributed to two factors: (1) The energy dissipation due to compression of pore and fracture formation inside the sample; (2) the weakening of the mechanical properties of samples leading to greater deformation under loading, causing energy dissipation.

3.2.4 Failure pattern

The failure patterns of samples with $ScCO_2$-water-coal reaction are shown in Fig. 10. Under different confining pressures and reaction times, the samples exhibit distinct failure patterns. It can be observed that samples without the $ScCO_2$-water-coal reaction slide along a primary shear plane after failure, without generating branching fracture surfaces, displaying an overall brittle shear failure pattern. After 7 days of the $ScCO_2$-water-coal reaction, in addition to the primary shear sliding surface, the samples develop numerous branching fracture surfaces around, resulting in a more complex failure morphology. After 14 days of the $ScCO_2$-water-coal reaction, the NM sample exhibits a similar post-failure morphology as observed after 7 days of the reaction, but with more and longer branching fracture surfaces. In contrast, the SX sample demonstrates a significantly different failure pattern with no primary shear sliding surface, but instead with numerous fracture surfaces that are approximately parallel to the axial direction of the sample.

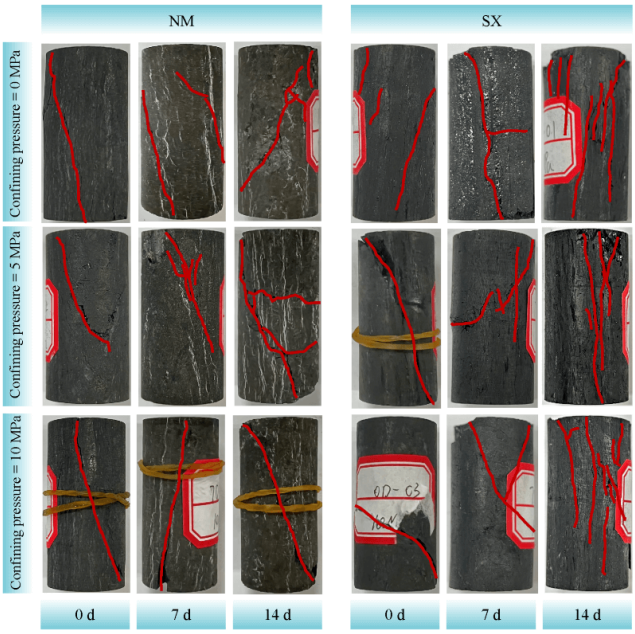

Fig. 10. Failure pattern of samples under the $ScCO_2$-water-coal reaction.

The confining pressure restricts the lateral deformation of samples during the loading process, simplifying the failure morphology and somewhat mitigating the changes in the failure pattern induced by the $ScCO_2$-water-coal reaction. Overall, after the $ScCO_2$-water-coal reaction, the failure pattern of the NM sample transitions from monoclinic shearing to an approximately X-shaped shearing, displaying a brittle-ductile characteristic. On the other hand, the failure pattern of the SX sample shifts from monoclinic shearing to approximately X-shaped shearing and to plastic failure, indicating a stronger plastic characteristic. This is due to the strong extracting ability of $ScCO_2$, which can significantly soften the organic matter. The NM sample has low organic matter content and high soluble mineral content, making the damaged pores and fractures formed after the $ScCO_2$-water-coal reaction becomes the starting point for fracture surface development. Conversely, the SX sample contains a large amount of organic matter, and after reacting with $ScCO_2$, the macromolecule structure is disrupted, leading to the manifestation of the flow-plasticization phenomenon during the loading process.

3.3 Influence of $ScCO_2$-water-coal reaction on microscopic mechanical behavior of coal

3.3.1 Nanoindentation load-displacement curves

The nanoindentation load-displacement curves of samples with $ScCO_2$-water-coal reaction are shown in Fig. 11. The curves of NM and SX samples before and after the reaction in $ScCO_2$-water-coal reaction show similar evolution laws, but under the same nanoindentation conditions, the maximum indentation depth (h_{max}) varies significantly. As the reaction time increases from 0 to 7d and to 14 d, the h_{max} of the NM sample ranges from 1,546.2-1,654.6 nm, to 1,623.5-1,754.4 nm, and to 1,759.7-1,923.5 nm, with average enhancements of 6.80% and 16.32%; while the h_{max} of the SX sample ranges from 1,625.7-2176.4 nm, to 2,195.1-2,261.7 nm, and to 2,389.3-2,637.9 nm, with average enhancements of 14.78% and 29.77%. These figures confirm the mechanical weakening effect of the $ScCO_2$-water-coal reaction at the microscale. Moreover, samples with greater h_{max} exhibit larger residual indentation depth after unloading, indicating that the $ScCO_2$-water-coal reaction enhances the irreversible deformation and reduces the elastic recovery ability of samples.

3.3.2 Creep time-displacement curve

Nanoindentation tests can rapidly determine the creep properties of small-volume samples, reflecting the macroscopic creep behavior of coal seams during long-term $ScCO_2$ sequestration processes (Memon et al., 2024). The creep curves of samples that underwent the $ScCO_2$-water-coal reaction are shown in Fig. 12. The nanoindentation creep curves of samples can be divided into transient stage and steady-state stage, with more pronounced stage changes observed in the NM sample. These samples reach creep equilibrium in a short period, with the creep displacement remaining relatively constant. This phenomenon intensifies with the extension of the $ScCO_2$-water-coal reaction. Conversely, the SX sample exhibits more distinct creep behavior and require a longer time to reach equilibrium, which indicates that samples tend to plasticize after the $ScCO_2$-water-coal reaction. The NM sample retains some elastic characteristics, while the SX sample shows more pronounced plasticization. Additionally, the NM sample shows a decrease in creep displacement, caused by elastic recovery due to stress relaxation in localized areas of the sample (Liu et al., 2019). This reflects the strong heterogeneity that persists in samples after the $ScCO_2$-water-coal reaction.

3.3.3 Microscopic mechanical parameters

As the $ScCO_2$-water-coal reaction time increases from 0 to 7 d and to 14 d, the average nanoindentation modulus of the NM sample decreases from 5.79 to 4.61 GPa and to 4.27 GPa, corresponding to a reduction of 20.38% and 26.25%, respectively; that of the SX sample decreases from 3.94 to 3.28 GPa and to 2.92 GPa, corresponding to a reduction of 16.75% and 25.89%, respectively. The average hardness of the NM sample decreases from 864.23 to 548.94 MPa and to 421.29 MPa, corresponding to a reduction of 36.48% and 51.25%, respectively, and that of the SX sample decreases from 416.86 to 245.69 MPa and to 185.03 MPa, corresponding to a reduction of 41.06% and 55.61%, respectively. Overall, both before and after the $ScCO_2$-water-coal reaction, the nanoindentation modulus and hardness of the NM sample are higher than those of the SX sample, consistent with the macroscopic mechanical parameters. However, the reduction amplitude in indentation modulus and hardness differ, for the following main reasons: (1) The microscopic mechanical parameters cannot fully describe the macroscopic mechanical behavior of samples because they cannot reflect both the spatial distribution of organic and mineral matter and the effect of pores and fractures in samples; (2) due to the scale difference between the microscopic and macroscopic levels, a large amount of microscopic mechanical parameter data

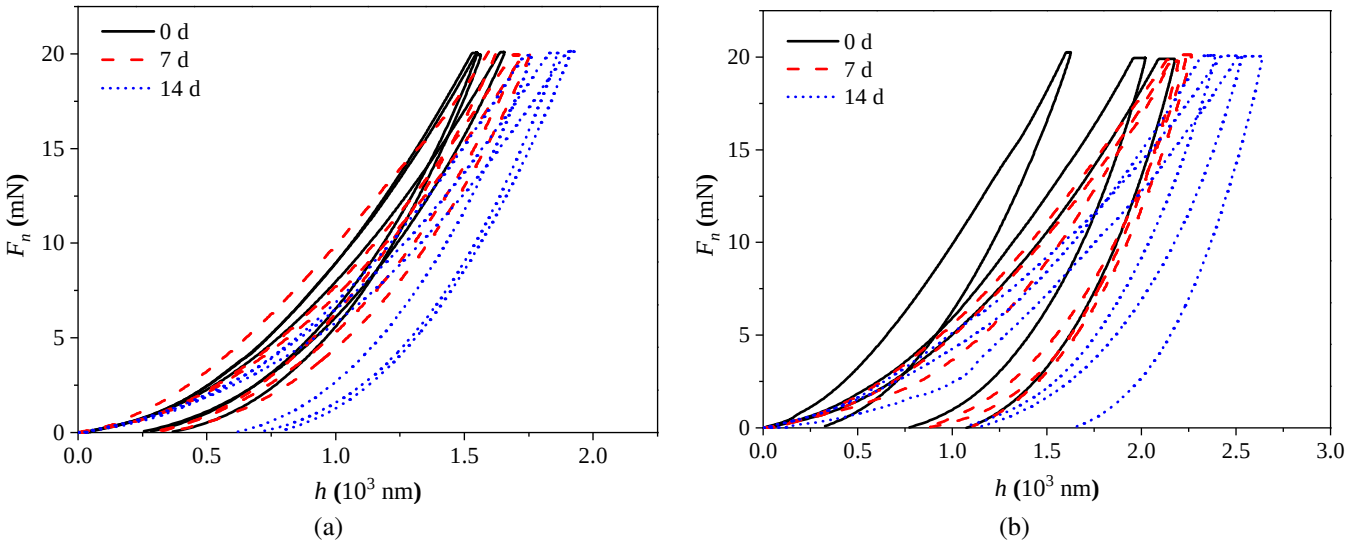

Fig. 11. Nanoindentation load-displacement curves of samples under the $ScCO_2$-water-coal reaction. (a) and (b) represent NM and SX samples, respectively.

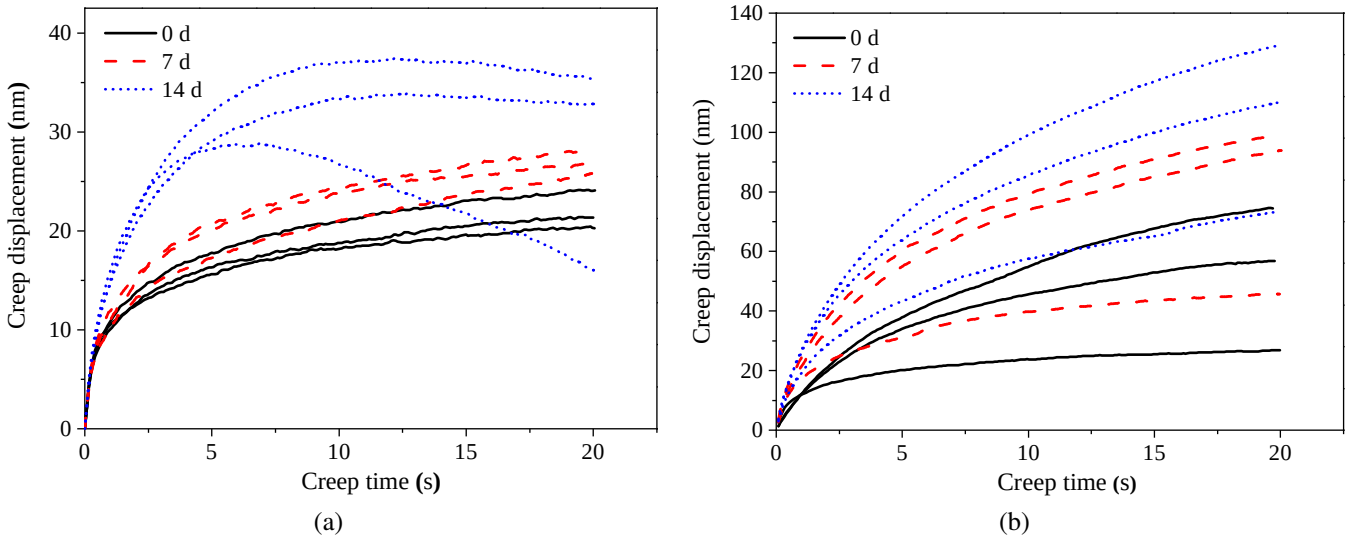

Fig. 12. Creep curves of samples undergoing the $ScCO_2$-water-coal reaction. (a) and (b) represent NM and SX samples, respectively.

is required for statistical analysis to accurately reflect the macroscopic characteristics of samples.

3.4 Macro-microscopic softening mechanism and safety response of coal

The macro-microscopic softening effect observed after injecting $ScCO_2$ into coal seams can be attributed to changes in their microscopic pore and fracture structures, stemming from the physicochemical interactions between $ScCO_2$, water and coal. In terms of chemical reactions, CO_2 dissolves in water to form carbonic acid, which can dissolve quartz, calcium carbonate, dolomite, and kaolinite, leading to the precipitation of quartz (Alhammad et al., 2024). This geological process has also been corroborated by previous studies (Dong et al., 2024; Hu et al., 2024) (Eqs. (12)-(16)). Thus, it can be considered as a primary cause of the formation of new pores and fractures. Moreover, the extraction of coal macromolecular structures by $ScCO_2$ causes structural damage, thereby enhancing the plastic characteristics of coal seams (Hosseinzadeh et al., 2024):

$$CO_2 + H_2O \leftrightarrow H_2CO_3 \leftrightarrow H^+ + HCO_3^- \quad (12)$$

$$\text{Quartz} + 4H^+ \leftrightarrow Si^{4+} + H_2O \quad (13)$$

$$\text{Calcite} + 2H^+ \leftrightarrow Ca^{2+} + 2H_2O + 2CO_2 \quad (14)$$

$$\text{Dolomite} + 4H^+ \leftrightarrow Ca^{2+} + Mg^{2+} + 2H_2O + 2CO_2 \quad (15)$$

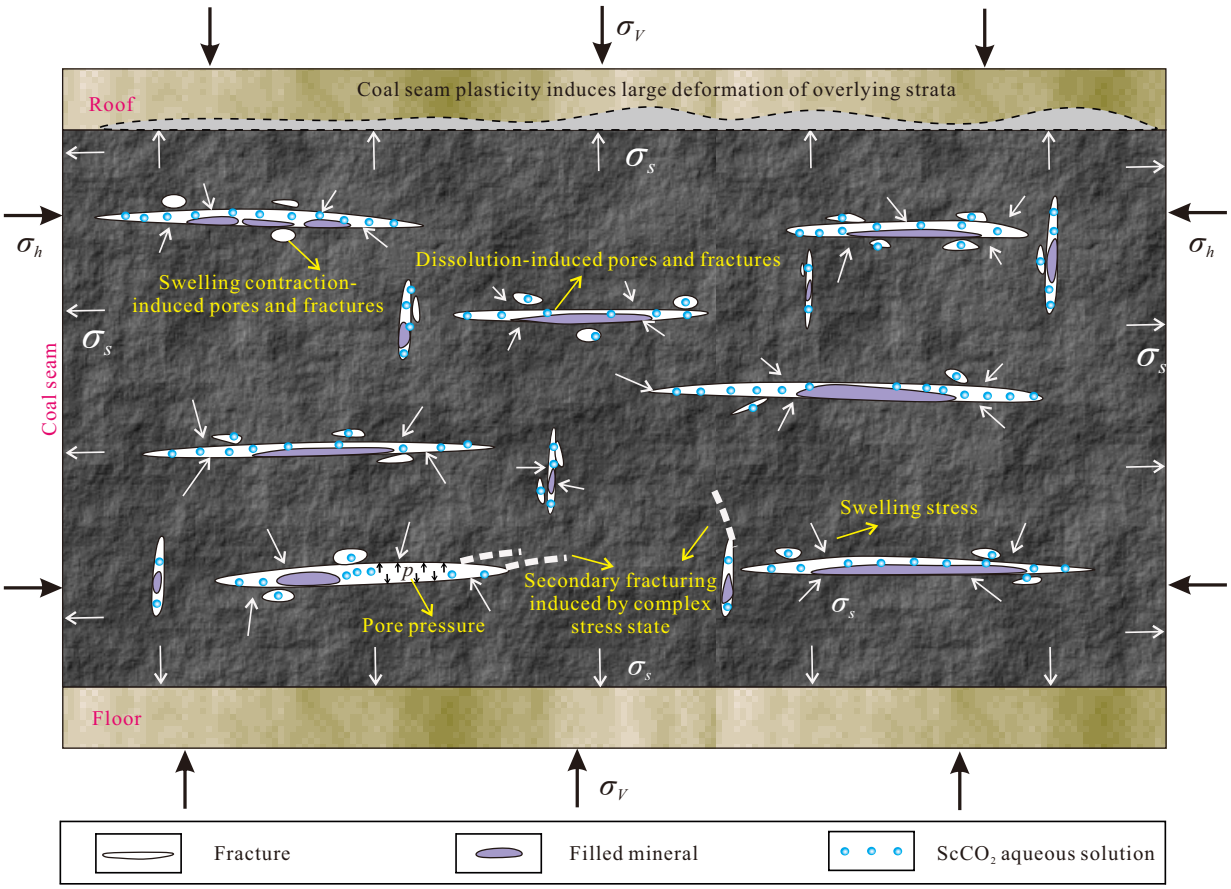

Fig. 13. Schematic diagram of CO_2 sequestration security issues in deep coal seams induced by the $ScCO_2$-water-coal reaction. Note: σ_V and σ_h are the vertical and horizontal stresses, respectively.

$$\text{Kaolinite} + 6H^+ \leftrightarrow 2Al^{3+} + 5H_2O + 2SiO_2 \quad (16)$$

In terms of physical effects, clay minerals exhibit a water-swelling effect, and their propensity for interlayer sliding is one of the factors contributing to the plastic deformation of the internal structure of coal seams under $ScCO_2$ injection (Cheng et al., 2022). The absorption of $ScCO_2$ by the coal matrix leads to swelling deformation, which induces swelling stress (σ_s) (Eq. (17)) (Connell and Detournay, 2009), altering the internal stress state of the coal seam:

$$\sigma_s = \frac{2a_m \rho RT \ln(1 + b_m p)}{3V_m} \quad (17)$$

where a_m represents the limit adsorption capacity, b_m represents the adsorption equilibrium constant, ρ represents the apparent density of coal, R represents the general gas constant, T represents the absolute temperature, and V_m is the molar volume.

According to the Mohr-Coulomb criterion, the critical shear strength (τ_s) regarding the failure of discontinuities in coal seams can be expressed by Eq. (18). The effective stress (σ) is composed of the total geostress (σ_g), reservoir pressure (p), and swelling stress (Liu and Rutqvist, 2010):

$$\begin{cases} \tau_s = c + \sigma \tan \varphi \\ \sigma = \sigma_g - p - \sigma_s \end{cases} \quad (18)$$

where c and φ respectively represent the cohesion and internal friction angle of the coal seam.

Injecting $ScCO_2$ can induce chemical dissolution and the swelling stress effect, leading to the formation of fractures and the occurrence of brittle failure, which is accompanied by a significant decrease in the cohesion and internal friction angle, as discussed above. This effect is magnified in deeper coal seams where reservoir pressure is promoted and coal swelling stress rises as a logarithmic function (Salmachi et al., 2023). Under these conditions, the critical shear strength along discontinuities in the coal seam declines sharply, thereby increasing the likelihood of internal fracturing and leakage during $ScCO_2$ sequestration.

Furthermore, processes such as solvent extraction, the interlayer sliding of clay minerals, and swelling deformation enhance the plastic characteristics of the coal seam, resulting in its reduced load-bearing capacity. In a complex stress environment characterized by high tectonic stress, reservoir pressure and swelling stress, the overlying strata may fracture and deform (Fig. 13) (Liu et al., 2023b; Wetzel et al., 2023). This in turn can lead to land displacements at the surface, po-

tentially impacting man-made structures and the environmental ecosystem (Ferronato et al., 2010). Thus, the macroscopic disasters induced by CO_2 sequestration are the result of the gradual amplification and manifestation of the microscopic responses triggered. Consequently, safety evaluation is particularly important, especially considering the long-term attribute of CO_2 sequestration in deep coal seams.

4. Conclusions

1) During the first 7 days of the $ScCO_2$-water-coal reaction, the pore-fracture structure in coal is modified significantly. After this reaction, original fractures in the coal reopen, the original micro-fractures expand, and new fractures form under the influence of chemical dissolution and adsorption-induced swelling and contraction. The pores evolve from small to large and link with fractures, i.e., large fractures promote the formation of the surrounding associated pores and micro-fractures; conversely, they can obstruct pore formation and result in a non-homogeneous distribution of pores if they intersect at an angle with the flow direction.
2) As a result of the $ScCO_2$-water-coal reaction, the peak strength, elastic modulus, internal friction angle, and cohesion are reduced, the Poisson's ratio is increased, and the energy dissipation during loading is advanced. The nanoindentation modulus and hardness of samples are significantly decreased, and the irreversible deformation upon unloading is enhanced. The changes in the micromechanical parameters align with those in the macromechanical ones, confirming the softening effect of the $ScCO_2$-water-coal reaction on coal at different scales. However, due to the strong heterogeneity of coal and the inability of microscopic parameters to reflect the component and pore-fracture distribution in coal, there are inconsistent characteristics in the change amplitude of macroscopic and microscopic mechanical parameters.
3) The threats of ground deformation and leakage faced by $ScCO_2$ sequestration in deep coal seams can be comprehensively considered at the micro, meso and macro levels. At the microscopic level, the main processes are the $ScCO_2$ extraction of organic matrix and chemical dissolution. At the mesoscopic level, the main process is the evolution of pores and fractures at different scales. At the mesoscopic level, the main process is the coupling effect of geostress, reservoir pressure and swelling stress. The linkage effect at different scales leads to potential safety issues in the $ScCO_2$ sequestration in deep coal seams.

Acknowledgements

This study was funded by the Hebei Natural Science Foundation (Nos. A2024210057 and E2021210128), the National Natural Science Foundation of China (No. 12372375), and the Science and Technology Research and Development Plan of Shijiazhuang (No. 241791097A).

Conflict of interest

The authors declare no competing interest.

Open Access This article is distributed under the terms and conditions of the Creative Commons Attribution (CC BY-NC-ND) license, which permits unrestricted use, distribution, and reproduction in any medium, provided the original work is properly cited.

References

Alhammad, F., Ali, M., Yekeen, N. P., et al. The effect of methylene blue and organic acids on the wettability of sandstone formation: Implications for enhanced oil recovery. Capillarity, 2024, 10(2): 29-37.

Anderson, S. T. Risk, liability, and economic issues with long-term CO_2 storage-a review. Natural Resources Research, 2017, 26(1): 89-112.

Anggara, F., Sasaki, K., Sugai, Y. Mineral Dissolution/precipitation during CO_2 injection into coal reservoir: A laboratory study. Energy Procedia, 2013, 37: 6722-6729.

Bekeshov, D., Ashimov, S., Wang, Y., et al. Understanding gas-enhanced methane recovery in graphene nanoslits via molecular simulations. Capillarity, 2023, 6(1): 1-12.

Busch, A., Gensterblum, Y. CBM and CO_2-ECBM related sorption processes in coal: A review. International Journal of Coal Geology, 2011, 87(2): 49-71.

Chang, R., Kim, S., Lee, S., et al. Calcium carbonate precipitation for CO_2 storage and utilization: A review of the carbonate crystallization and polymorphism. Frontiers in Energy Research, 2017, 5: 17.

Chen, B., Li, S., Tang, D., et al. Evaluation of recoverable potential of deep coalbed methane in the Linxing Block, Eastern Margin of the Ordos Basin. Scientific Reports, 2024, 14(1): 9192.

Cheng, P., Zhang, C., Ma, Z., et al. Experimental study of micromechanical properties alterations of shale matrix treated by $ScCO_2$-Water saturation using nanoindentation tests. Energy, 2022, 242: 122965.

Connell, L. D., Detournay, C. Coupled flow and geomechanical processes during enhanced coal seam methane recovery through CO_2 sequestration. International Journal of Coal Geology, 2009, 77(1): 222-233.

Dong, L., Liu, X., Gong, B., et al. Geomechanical properties of hydrate-bearing strata and their applications. Advances in Geo-Energy Research, 2024, 11(3): 161-167.

Du, Q., Liu, X., Wang, E., et al. Effects of CO_2-water interaction with coal on mineral content and pore characteristics. Journal of Rock Mechanics and Geotechnical Engineering, 2020, 12(2): 326-337.

Espinoza, D. N., Santamarina, J. C. CO_2 breakthrough—Caprock sealing efficiency and integrity for carbon geological storage. International Journal of Greenhouse Gas Control, 2017, 66: 218-229.

Ferronato, M., Gambolati, G., Janna, C., et al. Geomechanical issues of anthropogenic CO_2 sequestration in exploited gas fields. Energy Conversion and Management, 2010, 51(10): 1918-1928.

Fu, C., Du, Y., Song, W., et al. Application of automated mineralogy in petroleum geology and development and

CO_2 sequestration: A review. Marine and Petroleum Geology, 2023, 151: 106206.

Fujioka, M., Yamaguchi, S., Nako, M. CO_2-ECBM field tests in the Ishikari Coal Basin of Japan. International Journal of Coal Geology, 2010, 82(3): 287-298.

Gholami, R., Raza, A., Iglauer, S. Leakage risk assessment of a CO_2 storage site: A review. Earth-Science Reviews, 2021, 223: 103849.

Gor, G. Y., Huber, P., Bernstein, N. Adsorption-induced deformation of nanoporous materials-a review. Applied Physics Reviews, 2017, 4(1): 011303.

He, H., Liu, P., Nie, B., et al. Micromechanical property evolution and damage mechanism of coal subjected to $ScCO_2$ treatment. Energy, 2024, 304: 132087.

Hosseinzadeh, S., Haghighi, M., Salmachi, A., et al. Carbon dioxide storage within coal reservoirs: A comprehensive review. Geoenergy Science and Engineering, 2024, 241: 213198.

Hu, M., Niu, Q., Yuan, W., et al. Evolution characteristics and mechanism of microstructure, hydraulic and mechanical behaviors of sandstone treated by acid-rock reaction: Application of in-situ leaching of uranium deposit. Journal of Hydrology, 2024, 643: 131948.

Ibrahim, A. F. Prediction of coal wettability using machine learning for the application of CO_2 sequestration. International Journal of Greenhouse Gas Control, 2022, 118: 103670.

Jia, J. Experimental simulation on stress and strain effects as supercritical CO_2 being injected into deep anthracite reservoirs. Xuzhou, China University of Mining and Technology, 2017. (in Chinese)

Jia, J., Cao, L., Sang, S., et al. An experimental study on the damage characteristics of mechanical properties of anthracite induced by supercritical CO_2 injection. Environmental Earth Sciences, 2019, 79(1): 12.

Ji, Z., Chen, Z., Pan, J., et al. A novel method for estimating methane emissions from underground coal mines: The Yanma coal mine, China. Atmospheric Environment, 2017, 170: 96-107.

Li, K., Zhu, C., Wan, J., et al. Experimental investigation into coal wettability changes caused by reactions with $scCO_2$-H_2O. Gas Science and Engineering, 2024, 128: 205366.

Liu, A., Liu, S., Liu, Y., et al. Characterizing mechanical heterogeneity of coal at nano-to-micro scale using combined nanoindentation and FESEM-EDS. International Journal of Coal Geology, 2022, 261: 104081.

Liu, C. J., Wang, G. X., Sang, S. X., et al. Changes in pore structure of anthracite coal associated with CO_2 sequestration process. Fuel, 2010, 89 (10): 2665-2672.

Liu, H., Rutqvist, J. A new coal-permeability model: Internal swelling stress and fracture-matrix interaction. Transport in Porous Media, 2010, 82(1): 157-171.

Liu, K., Ostadhassan, M., Xu, X., et al. Abnormal behavior during nanoindentation holding stage: Characterization and explanation. Journal of Petroleum Science and Engineering, 2019, 173: 733-747.

Liu, X., Jia, X., Liu, W., et al. Mechanical strength and porosity changes of bituminous coal induced by supercritical CO_2 interactions: Influence of saturation pressure. Geoenergy Science and Engineering, 2023a, 225: 211691.

Liu, X., Sang, S., Zhou, X., et al. Modelling of geomechanical response for coal and ground induced by CO_2-ECBM recovery. Gas Science and Engineering, 2023b, 113: 204953.

Ma, Z., Pathegama Gamage, R., Zhang, C. Application of nanoindentation technology in rocks: A review. Geomechanics and Geophysics for Geo-Energy and Geo-Resources, 2020, 6: 60.

Memon, S., Verrall, M., Lebedev, M., et al. Nanoscale analysis of shale matrix alteration after supercritical CO_2 treatment: Implications for $scCO_2$ fracturing in shales. Energy & Fuels, 2024, 38(3): 1873-1890.

Meng, Z., Zhang, J., Wang, R. In-situ stress, pore pressure and stress-dependent permeability in the Southern Qinshui Basin. International Journal of Rock Mechanics and Mining Sciences, 2011, 48(1): 122-131.

Niu, Q., Cao, L., Sang, S., et al. Experimental study on the softening effect and mechanism of anthracite with CO_2 injection. International Journal of Rock Mechanics and Mining Sciences, 2021a, 138: 104614.

Niu, Q., Cao, L., Sang, S., et al. A small-scale experimental study of CO_2 enhanced injectivity methods of the high-rank coal. Petroleum Science, 2021b, 18(5): 1427-1440.

Niu, Q., Wang, Q., Wang, W., et al. Responses of multi-scale microstructures, physical-mechanical and hydraulic characteristics of roof rocks caused by the supercritical CO_2-water-rock reaction. Energy, 2022, 238: 121727.

Otu, S., Rinehart, A. J., Luhmann, A. J., et al. Effects of CO_2 on creep deformation in sandstones at carbon sequestration reservoir conditions: an experimental study. International Journal of Greenhouse Gas Control, 2023, 129: 103970.

Pan, J., Jiao, F., Wang, K., et al. Molecular simulations of the effects of CO_2 and N_2 injection on CH_4 adsorption, coal porosity and permeability. Advances in Geo-Energy Research, 2024, 12(3): 205-222.

Perera, M. S. A., Ranjith, P. G., Viete, D. R. Effects of gaseous and super-critical carbon dioxide saturation on the mechanical properties of bituminous coal from the Southern Sydney Basin. Applied Energy, 2013, 110: 73-81.

Salmachi, A., Zeinijahromi, A., Algarni, M. S., et al. Experimental study of the impact of CO_2 injection on the pore structure of coal: A case study from the Bowen Basin, Australia. International Journal of Coal Geology, 2023, 275: 104314.

Sampath, K. H. S. M., Perera, M. S. A., Elsworth, D., et al. Experimental investigation on the mechanical behavior of victorian brown coal under brine saturation. Energy & Fuels, 2018, 32(5): 5799-5811.

Sampath, K. H. S. M., Perera, M. S. A., Elsworth, D., et al. Effect of coal maturity on CO_2-based hydraulic fracturing process in coal seam gas reservoirs. Fuel, 2019a, 236: 179-189.

Sampath, K. H. S. M., Perera, M. S. A., Ranjith, P. G.,

et al. Qualitative and quantitative evaluation of the alteration of micro-fracture characteristics of supercritical CO_2-interacted coal. The Journal of Supercritical Fluids, 2019b, 147: 90-101.

Sang, S., Niu, Q., Cao, L., et al. Mechanical response characteristics and mechanism of coal-rock with CO_2 injection in deep coal seam: A review. Earth Science, 2022, 47(5): 1849-1864. (in Chinese)

Song, H., Zhong, Z., Lin, B. Chemical dissolution of minerals in anthracite after supercritical carbon dioxide immersion: Considering mechanical damage and enhanced porosity. Energy, 2023a, 283: 129063.

Song, Y., Jun, S., Na, Y., et al. Geomechanical challenges during geological CO_2 storage: A review. Chemical Engineering Journal, 2023b, 456: 140968.

Wang, H., Cheng, X., Tian, J., et al. Permeability enhancement of low rank coal through acidization using H_2S solution: An experimental study in the Kuqa-Bay Coalfield, Xinjiang, China. Journal of Petroleum Science and Engineering, 2020a, 185: 106476.

Wang, H., Xiang, J., Deng, X., et al. Micromechanical properties of coals and the response to changes in nanocarbon structure. Fuel, 2024, 373: 132321.

Wang, W., Wang, H., Fan, Y., et al. Distribution characteristics and enrichment factor gallium in coal seam No. 4 in Majialiang-Fangziping area, Fugu mining area. Paper Presented at the 4th International Symposium on Resource Exploration and Environmental Science, Ordos, China, 25-26 April, 2020b.

Wei, Y., Li, Z., Chen, B., et al. A numerical simulation study on the evolutionary characteristics of the damage process of karst soil cavity under positive pressure effect. Geohazard Mechanics, 2023, 1(4): 288-296.

Wetzel, M., Otto, C., Chen, M., et al. Hydromechanical impacts of CO_2 storage in coal seams of the Upper Silesian Coal Basin (Poland). Energies, 2023, 16(7): 3279.

Xue, Y., Ranjith, P. G., Dang, F., et al. Analysis of deformation, permeability and energy evolution characteristics of coal mass around borehole after excavation. Natural Resources Research, 2020, 29(5): 3159-3177.

Xu, J., Luo, S., Xiao, X., et al. Review of the experimental studies of the cracking behaviors of fractured rocks under compression. Geohazard Mechanics, 2024, 2(2): 59-82.

Zagorščak, R., Thomas, H. R. Effects of subcritical and supercritical CO_2 sorption on deformation and failure of high-rank coals. International Journal of Coal Geology, 2018, 199: 113-123.

Zhang, F., Jiao, Y., Wang, S., et al. Origin of dispersed organic matter within sandstones and its implication for uranium mineralization: A case study from Dongsheng uranium ore filed in China. Journal of Earth Science, 2022a, 33(2): 325-341.

Zhang, G., Ranjith, P. G., Fu, X., et al. Pore-fracture alteration of different rank coals: Implications for CO_2 sequestration in coal. Fuel, 2021a, 289: 119801.

Zhang, G., Ranjith, P. G., Li, Z., et al. Long-term effects of CO_2-water-coal interactions on structural and mechanical changes of bituminous coal. Journal of Petroleum Science and Engineering, 2021b, 207: 109093.

Zhang, G., Ranjith, P. G., Lyu, Q. Direct evidence of CO_2 softening effects on coal using nanoindentation. Energy, 2022b, 254: 124221.

Zhou, X., Sang, S., Niu, Q., et al. Changes of multiscale surface morphology and pore structure of mudstone associated with supercritical CO_2-water exposure at different times. Energy & Fuels, 2021, 35(5): 4212-4223.